Visualizing the diversity of representations learned by *Bayesian* neural networks

Anonymous authors
Paper under double-blind review

Abstract

Explainable Artificial Intelligence (XAI) aims to make learning machines less opaque, and offers researchers and practitioners various tools to reveal the decision-making strategies of neural networks. In this work, we investigate how XAI methods can be used for exploring and visualizing the diversity of feature representations learned by *Bayesian* neural networks (BNNs). Our goal is to provide a global understanding of BNNs by making their decision-making strategies a) visible and tangible through feature visualizations and b) quantitatively measurable with a distance measure learned by contrastive learning. Our work provides new insights into the *posterior* distribution in terms of human-understandable feature information with regard to the underlying decision-making strategies. Our main findings are the following: 1) global XAI methods can be applied to explain the diversity of decision-making strategies of BNN instances, 2) Monte Carlo dropout with commonly used Dropout rates exhibit increased diversity in feature representations compared to the multimodal posterior approximation of MultiSWAG, 3) the diversity of learned feature representations highly correlates with the uncertainty estimate for the output and 4) the inter-mode diversity of the multimodal posterior decreases as the network width increases, while the intra-mode diversity increases. Our findings are consistent with the recent deep neural networks theory, providing additional intuitions about what the theory implies in terms of humanly understandable concepts.

1 Introduction

Despite the great success of deep neural networks (DNN), little is known about the decision-making strategies that they have learned. This lack of transparency is a major cause of concern since DNNs are being used in safety-critical applications (Berkenkamp et al., 2017; Huang & Chen, 2020; Le et al., 2021) and it has been shown that they tend to encode fallacies, including the memorization of spurious correlations (Lapuschkin et al., 2019; Izmailov et al., 2022) or being biased towards the data set that they were trained on (Tommasi et al., 2017; Turner Lee, 2018; Ribeiro et al., 2016). Therefore, in recent years, the field of explainable artificial intelligence (XAI) has established itself in order to make the decisions of AI models comprehensible to humans. XAI methods allow the user to "open" the black-box of trained neural networks, that is, understanding what the model has learned and on which features its decisions are based.

Such *post-hoc* XAI methods can be further categorized into *local* and *global* explanation methods. While *local* XAI methods assign importance scores to input features, e.g. image pixels, that are important for a model's prediction (Bykov et al., 2021a; Sundararajan et al., 2017; Simonyan et al., 2013; Lapuschkin et al., 2015; Rs et al., 2017; Smilkov et al., 2017), *global* XAI methods aim to explain the inner workings of a DNN, e.g. what concepts are encoded in its parameters, by providing *feature visualizations* (FVs) (Olah et al., 2017; 2018; Bau et al., 2020). XAI methods have been applied extensively on many deep neural network types that were trained in a *frequentist* fashion, namely convolutional neural networks (Lecun et al., 1998), recurrent neural networks (Medsker & Jain, 1999), and others (Hilton et al., 2020; Schnake et al., 2021; Bau et al., 2020). In a recent work Bykov et al. (2021b), those methods have been applied to neural networks that were trained in a *Bayesian* fashion. Inherently, *Bayesian* neural networks (BNN) offer the property of uncertainty estimation that results from the diversity of learned feature representations and prediction strategies of different BNN instances. We will refer to these prediction strategies as decision-making strategies. In their work Bykov et al.

(2021b) the authors apply *local* explanation methods on top of BNN instances and obtain a distribution over explanations, from which they estimate explanation uncertainties. Our work builds up on this idea, and aims to answer the following questions:

1. Can the diversity of BNN instances be explained by *global* XAI methods?
2. Does the choice of the *Bayesian* inference method affects the diversity of their feature visualization?
3. Can the uncertainty estimates provided by a BNN be explained by the diversity of their feature visualizations?
4. How does the network width affects the diversity of explanations of samples from a multimodal posterior distribution?

To the extent of our knowledge, we are the pioneers in utilizing *global* XAI techniques to explain the diversity of BNN instances. Our findings provide empirical support to the recent advancements in deep learning theory (Roberts et al., 2021) and illustrate these principles in a novel manner.

2 Background

In this section, we provide a brief overview of *Bayesian* neural networks and global explanation methods, which are used in the following work.

2.1 *Bayesian* neural networks

Bayesian machine learning estimates the posterior distribution over unknown variables rather than estimating a single value. We focus on neural network classifiers, where the conditional distribution of the model is given as

$$p(y|x,\theta) = \text{SoftMax}(f_\theta(x)), \tag{1}$$

with $f_\theta(x)$ being the network function parameterized with θ. Let $\mathcal{D} := \{(x^{(1)}, y^{(1)}), \ldots, (x^{(N)}, y^{(N)})|\ x^{(n)} \in \mathbb{R}^D,\ y^{(n)} \in \{0,1\}^C\ \forall n = 1, \ldots, N\}$ be a training data set, where N is the number of training samples, and C is the number of distinct classes. The label $y^{(n)}$ is a one-hot encoded vector, where the vector-entry corresponding to the correct class is one and the rest is set to zero. Given a *prior distribution* $p(\theta)$ on the network parameter, the *posterior* distribution is given by Bayes' theorem (Pearson et al., 1959):

$$p(\theta|\mathcal{D}) = \frac{p(\mathcal{D}|\theta)p(\theta)}{p(\mathcal{D})} = \frac{p(\mathcal{D}|\theta)p(\theta)}{\int p(\mathcal{D}|\theta)p(\theta)d\theta}. \tag{2}$$

Then, the *predictive* distribution $p(y^*|x^*, \mathcal{D})$ for a test point x^* is given by marginalizing over all possible model parameter setups:

$$p(y^*|x^*, \mathcal{D}) = \int p(y^*|x^*, \theta)p(\theta|\mathcal{D})d\theta, \tag{3}$$

encoding the models uncertainty regarding the predicted label y^* for a given test point x^*.

Since the integrals in equation 2 and equation 3 are computationally intractable for DNNs, several approximation methods have been proposed (Mackay et al., 1999; Neal & Neal, 2021; Graves, 2021; Blundell et al., 2015; Zhang et al., 2019). For the latter we can draw samples from an approximate posterior $q(\theta|\mathcal{D}) \approx p(\theta|\mathcal{D})$, if the predictive distribution equation 3 can be approximated with T Monte Carlo samples:

$$p(y^*|x^*, \mathcal{D}) \approx \frac{1}{T}\sum_{t=1}^{T} p(y^*|x^*, \theta_t), \quad \theta_t \sim q(\theta|\mathcal{D}). \tag{4}$$

The resulting averaged output probability vector of the BNN is usually referred to as *Bayesian* model average (BMA). Below we introduce four popular methods for approximating the posterior with unimodal or multimodal distribution families.

2.1.1 Kronecker-Factored Approximation Curvature (KFAC)

KFAC (Martens & Grosse, 2015) approximates the true *posterior* distribution by learning the following *unimodal* multivariate normal distribution:

$$q_{\mathrm{MAP}}(\theta|\mathcal{D}) = \mathcal{N}(\theta; \hat{\theta}_{\mathrm{MAP}}, \hat{F}^{-1}),$$

where $\mathcal{N}(\mu, \Sigma)$ denotes the Gaussian distribution with mean μ and covariance Σ. The approximate posterior mean $\hat{\theta}_{\mathrm{MAP}}$ is the *maximum a posteriori* (MAP) estimate, which is obtained by a standard training algorithm such as stochastic gradient descent (SGD). The posterior covariance $\hat{F}^{-1}$ is the inverse of a regularized approximation of the Fisher information matrix F. For computational efficiency, the inverse Fisher information matrix $\hat{F}^{-1}$ is approximated by the sum of a diagonal matrix and a low-rank matrix expressed as a Kronecker factorization.

2.1.2 Monte-Carlo Dropout (MCDO)

Deep neural networks of arbitrary depth including non-linearities that are trained with dropout can be used to perform approximate *Bayesian* inference (Gal & Ghahramani, 2015). In MCDO, samples from the approximate posterior are drawn by

$$\theta_l = \theta_l^* \cdot diag([z_{l,m_l}]_{m_l=1}^{M_{l-1}}), \quad z_{l,m_l} \sim \mathrm{Bernoulli}(\gamma_l)$$

where θ_l^* is the weight matrix of layer l of dimensions $M_l \times M_{l-1}$ before Dropout is applied, $diag(\cdot)$ is a function that maps the vector $[z_{l,m_l}]_{m_l=1}^{M_{l-1}}$ to a diagonal matrix of dimension $M_{l-1} \times M_{l-1}$ with z_{l,m_l} being the diagonal element in row m_l and column m_l for $m_l = 1, ..., M_l$. The elements z_{l,m_l} are independent binary random variables that follow the Bernoulli distribution, e.g. $z_{l,m_l} \sim \mathrm{Bernoulli}(\gamma_l)$ and γ_l is the dropout rate. In practice, users can choose a fixed value of γ_l by optimizing some metric, e.g. the test accuracy.

2.1.3 Stochastic Weight Averaging Gaussian (SWAG)

SWAG (Maddox et al., 2019) is an efficient method to fit a Gaussian distribution around a local solution. The algorithm consists of an initial training phase followed by a model collection phase. During the training phase, the model is trained with SGD using a high constant learning rate. In the model collection phase, the SGD training continues for collecting SGD iterates. The trajectory of those iterates are then used to estimate the mean and the covariance of the approximate Gaussian *posterior* distribution:

$$q_{\mathrm{SWAG}}(\theta|\mathcal{D}) = \mathcal{N}(\theta; \hat{\theta}_{\mathrm{SWAG}}, \hat{\Sigma}_{\mathrm{SWAG}}).$$

The covariance $\hat{\Sigma}_{\mathrm{SWAG}}$ is approximated by the sum of a diagonal and a low-rank matrix, similarly to KFAC, for stable estimation from a small number of SGD iterates.

2.1.4 Deep Ensemble of SWAG (MultiSWAG)

MultiSWAG (Wilson & Izmailov, 2020) combines the ideas of SWAG and deep ensemble (Lakshminarayanan et al., 2016). It simply performs the SWAG training multiple times from different weight initializations, and each SGD trajectory is used to compute the mean $\hat{\theta}_k$ and the covariance $\hat{\Sigma}_k$ of a Gaussian distribution. The estimated Gaussians are combined to express the approximate posterior as a (equally-weighted) mixture of Gaussians (MoG):

$$q_{\mathrm{MultiSWAG}}(\theta|\mathcal{D}) = \frac{1}{K}\sum_{k=1}^{K} \mathcal{N}(\theta; \hat{\theta}_k, \hat{\Sigma}_k). \tag{5}$$

Since each SWAG trajectory is expected to converge to a different local solution or mode, MultiSWAG provides a *multimodal* approximation of the true *posterior*. MultiSWAG was shown to improve generalization performance and uncertainty estimation quality (Wilson & Izmailov, 2020).

Data set	image size	classes	Training size	Test size
Places365	$256 \times 256 \times 3$	365	∼1.4mil	365k
CIFAR-100	$32 \times 32 \times 3$	100	50k	10k

Table 1: Data sets used in the experiments.

Model	# Trainable parameters	Test accuracy
ResNet50	25,557,032	55.57%
WRes10	36,546,980	82.75%
WRes2	1,481,252	77.45%
WRes1 (*WideResNet28*)	376,356	72.57%
WRes0.7	88,448	62.54%
WRes0.2	5,008	27.96%

Table 2: Network architectures. WRes1 corresponds to the original *WideResNet28*, and WResβ for $\beta \neq 1$ is the network with the number of channels β times more than the original in each convolutional layer. The test accuracy is on Place365 for *ResNet50*, and on CIFAR100 for WResβ, respectively.

2.2 Global XAI methods

XAI methods that are decoupled from the architectural choice of a neural network or its training procedure are referred to as *post-hoc* XAI methods, which can be further categorised into *local* and *global* explanation methods. *Global* XAI methods aim to explain the general decision-making strategies learned by the representations of DNNs. They reveal the concepts to which a particular neuron responds the most (Olah et al., 2017; 2018; Bau et al., 2020; Nguyen et al., 2016) by decomposing and quantifying the activations of certain neural network layers in terms of human-understandable concepts (Kim et al., 2017; Koh et al., 2020), or by identifying and understanding causal relationships that are encoded between neurons (Reimers et al., 2020).

In this work, we focus on the activation maximization (AM) framework (Nguyen et al., 2016). The general idea of AM is to artificially generate an input that maximizes the activation of a particular neuron in a certain layer of a neural network. The optimization problem can be formulated as follows:

$$\hat{v} = \underset{v \in \mathbb{R}^V}{\operatorname{argmax}}\ a(v) + R(v), \tag{6}$$

where v is the input variable, $a(\cdot)$ is the activation of the neuron of interest, and $R(\cdot)$ is a regularizer. This can be easily extended to maximize the activation of a certain channel or layer by maximizing a norm of the channel's or layer's activation vectors. We refer to the resulting image, $\hat{v}$ in equation 6, as a feature visualization (FV) vector. In order to generate FV that are not full of high-frequency noise, as it is the case for adversarial examples (Szegedy et al., 2013; Goodfellow et al., 2014; Athalye et al., 2017), several regularization techniques have been proposed (Olah et al., 2017; Mordvintsev et al., 2018): *transformation robustness* applies several stochastic image transformations, e.g., jittering, rotating, or scaling, before each optimization step; *frequency penalization* either explicitly penalizes the variance between neighboring pixels or applies bilateral filters on top of the input. In order to even further reduce high-frequency patterns that correspond to noise, it was proposed to perform the optimization in a spatially decorrelated and whitened space, instead of the original image space. This space corresponds to the Fourier transformation of the image based on the spatially decorrelated colors. In this way, high frequency components are successfully reduced.

3 Experimental Setup

Here we describe our experimental setup including the methodologies for the quantitative analysis of feature visualizations.

Inference method	Test accuracy
KFAC	54.78%
MultiSWAG	56.64%
MCDO-5%	55.68%
MCDO-10%	55.07%
MCDO-25%	51.69%

Table 3: Approximate *Bayesian* inference methods analyzed in the experiments. Each inference method is based on a *ResNet50* model. For each inference method, the test accuracy on the Places365 test set is evaluated on the predictive distribution that we approximate with $T = 50$ MC samples.

3.1 Data sets

In our experiments, we use two data, Place365 and CIFAR-100, which are described in Tab. 1. When training a classifier, the Place365 images are clipped to $224 \times 224 \times 3$, and CIFAR100 images are kept in their original size of $32 \times 32 \times 3$.

3.2 Network Architectures

We train *ResNet50* (He et al., 2015) on Place365, and *WideResNet28* (Zagoruyko & Komodakis, 2016) on CIFAR100, respectively. To study the network width dependence, we also use *WideResNet28* with increased and decreased numbers of channels in each layer. Therefore, we scale the number of channels of the original *WideResNet28* by a scaling factor β, which we refer to as WResβ. For exampl, WRes2 corresponds to a network that is twice as wide as the original network. The number of parameters and the test accuracy are shown in Tab.2, where the test accuracies are obtained by evaluating the MAP estimates of the corresponding models.

3.3 Inference Methods

The approximate *Bayesian* inference methods that we analyzed are listed in Tab. 3. Each inference method is based on a *ResNet50* network architecture. MCDO-γ% is the MC dropout model with dropout rate γ%, applied to each layer of the CNN encoders except for the last one (same dropout rate for all layers). For MultiSWAG, the approximate posterior is a mixture equation 5 of $K = 10$ Gaussians. The test accuracy on the Places365 test set of each inference method is evaluated according to equation 4 with $T = 50$ MC samples.

3.4 Feature Visualization

In all experiments, we use the AM framework equation 6 to obtain the FV vectors, and analyze their behavior. The FV vector is by default of the same size as the input image. However, since the images in CIFAR-100 are small and therefore not very informative in terms of the concepts that we can extract from them qualitatively, we expand the input to $128 \times 128 \times 3$ using bilinear interpolation in PyTorch. We solve the AM optimization problem equation 6 by 512 steps of gradient descent with the step size of $\alpha = 0.05$. For regularization, we apply the transformation robustness with random rotation, random scaling, random jittering. Moreover, the optimization is performed in the decorrelated and whitened space. All transformations correspond to the default setting in (Olah et al., 2017), from which we used the PyTorch version of the published source code `https://github.com/greentfrapp/lucent`.

3.5 Quantitative Distance Measure in FV space

One of the main contributions of this work is to analyze the diversity of the "concepts", expressed in FV vectors, of BNN instances *quantitatively*. To this end, we need to define a distance measure in the space of FVs. Apparently, the standard norm distances, e.g. L2-distance and cosine-similarity, directly applied to the FV vectors is not appropriate since "concepts" in FV should be invariant to translations and rotations. We, therefore, use a non-linear function $g : \mathbb{R}^V \mapsto \mathbb{R}^Z$ that maps FV vectors into a low-dimensional *latent concept*

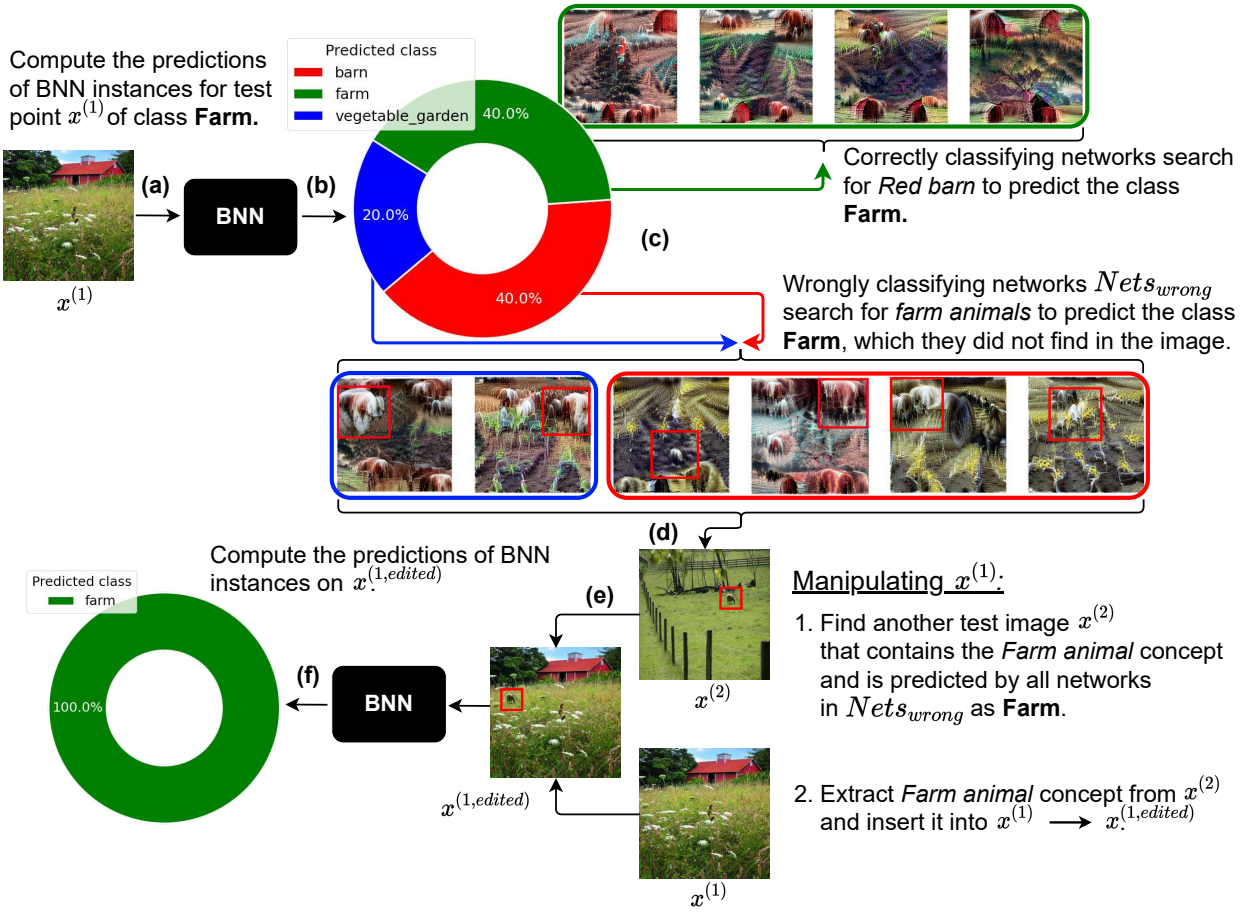

Figure 1: Explaining decision-making strategies of 10 individual BNN instances using FVs. (a) A test sample $x^{(1)}$ of class *Farm*. (b) 10 BNN instances classify $x^{(1)}$. (c) Classification results by 10 instances (only 40% classify $x^{(1)}$ correctly as *Farm*). FVs of the "correct" instances N_{correct} are shown in the upper green box, while those of the "wrong" instances N_{wrong} are in the lower blue and red boxes. We observe that FVs of N_{wrong} contain *Farm animal*-like concepts, which they did not find in the input $x^{(1)}$. (d) Another test sample $x^{(2)}$ that contains a tiny sheep. (e) We cut out the tiny sheep (*Farm animal* concept) patch from $x^{(2)}$ and paste it into $x^{(1)}$, yielding $x^{(1,\text{edited})}$. (f) All instances correctly classify $x^{(1,\text{edited})}$ as *Farm*, which implies that the FVs indeed encode human-understandable concepts that reflect the network's decision-making strategy.

space such that FVs with similar concepts are mapped to close points. Afterward, the distance between two FVs is measured by the cosine distance in this space:

$$d(v, v') = \frac{g(v)^\top g(v')}{\|g(v)\|\|g(v')\|}. \tag{7}$$

We learn the function g via a contrastive learning scheme (Chen et al., 2020; Li et al., 2020a;b), more specifically, we use the SimCLR framework (Chen et al., 2020).

Assume that we are given a training set $\{v_n\}_{n=1}^N$ of FVs. We first conduct stochastic data augmentation, which applies two random image transformations to each input, i.e., to each FV, resulting in M different versions of each input, which yields an augmented training set $\{\{\widetilde{v}_{n,m}\}_{m=1}^M\}_{n=1}^N$. Here $\{\widetilde{v}_{n,m}\}_{m=1}^M$ are generated by stochastic augmentation applied to the n-th original sample, e.g., v_n. Then, the non-linear map $g_\phi(\cdot)$ parameterized by ϕ is trained by minimizing the contrastive loss:

$$\sum_{n=1}^{N} \sum_{m,m'=1}^{M} \log \frac{\exp\left(\frac{d_\phi(\widetilde{v}_{n,m}, \widetilde{v}_{n,m'})}{\tau}\right)}{\sum_{n' \neq n} \sum_{m'',m'''=1}^{M} \exp\left(\frac{d_\phi(\widetilde{v}_{n,m''}, \widetilde{v}_{n',m'''})}{\tau}\right)}, \tag{8}$$

where d_ϕ is the distance measure equation 7 which depends on ϕ by $g_\phi(\cdot)$ and τ is a temperature hyperparameter. This contrastive loss aims to minimize the distances between the samples transformed from the same original test sample, while maximizing the distances between those transformed from different original test samples. For the architecutre of g_ϕ, we use a *ResNet18* (He et al., 2015) base encoder, that is, all *ResNet18* layers up to the average pooling layer, followed by a fully-connected layer, a *ReLU* non-linearity and another fully-connected layer. We use stochastic gradient descent (SGD), where the contrastive loss equation 8 with the batch size N and the temperature $\tau = 0.5$ is minimized in each epoch. The number of augmented samples is $M = 2$ (per original sample and epoch), and the augmentation is randomly chosen from "Random Cropping", "Colorjitter", and "Horizontal Flipping". We run SGD for 150 epochs on the CIFAR-100 based models, and for 250 epochs on the Places365 based models. For the contrastive learning we used the implementation of the following public repository `https://github.com/Yunfan-Li/Contrastive-Clustering`.

4 Experimental Results

In this section, we visualize and analyze the diversity of the decision-making strategies of BNN instances in terms of high-level concepts by using feature visualizations. In the first experiment, we demonstrate that the extracted FVs properly reflect the characteristics of each individual BNN model instance by relating FV to the classification prediction, and observing the model's uncertainty behavior when manipulating test samples. In the second experiment, we analyze the dependence between FVs and the initial parameter setting of the AM algorithm. In the third experiment, we analyze the correlation between the diversity of FVs and the uncertainty estimates of BNN model instances. While the first two experiments validate our methodology qualitatively, the third experiment confirms quantitatively that FVs reasonably reflect the property of a *Bayesian* ensemble. In the last two experiments, we use our distance measure to analyze the diversity of BNN instances from different posterior approximation methods, and different scale of models, which provide us with new insights into the latest findings of deep learning theory (Roberts et al., 2021). To the best of our knowledge, no previous work has used *global* XAI methods to explain the behavior of *Bayesian* neural networks instances.

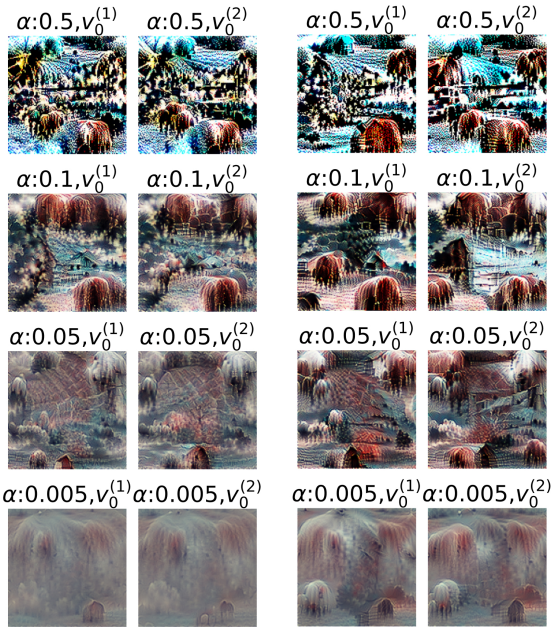

(a) 128 epochs (b) 512 epochs

Figure 2: Dependence of the FV on the number of epochs, the learning rate α, and the parameter initialization ($v_0^{(1)}$ or $v_0^{(2)}$). We observe that the number of epochs affects the color scheme slightly, the α affects the crispness and contrast drastically, and the parameter initialization affects the positions and shapes of objects slightly. However, the high-level concepts stay the same.

4.1 Visualizing characteristics of individual BNN instances

The prediction by a BNN is made from an ensemble of model instances drawn from the (approximate) posterior distribution, and such model instances can acquire different decision-making strategies. In this first experiment, we qualitatively show that by using FVs we are able to explain the diverse characteristics of each individual model instance in the *Bayesian* posterior ensemble. We draw model instances from the MCDO-5% posterior with the *ResNet50* architecture trained on Place365. To receive a global explanation for each of the 10 BNN instances for the class *Farm*, we apply the AM algorithm to the network output, maximizing the logit for the label *Farm*. From the 10 different FV images, shown in the green, blue and red boxes in Fig. 1, we can observe that all FV images contain reasonable high-level concepts, e.g., *Red barn*, *Farm animal*, *Tractor*, *Crop field*, and *Pasture fence*, implying that all BNN instances learned reasonable decision-making

strategies for the class *Farm*. However, we identify some test samples which are misclassified by some of the BNN instances.

One of the wrongly classified test samples, $x^{(1)}$, is shown in Fig. 1(a). Indeed, 4 of the instances classify $x^{(1)}$ correctly as *Farm*, while the other 6 instances classify it wrongly as either *Barn* or *Vegetable_garden* as shown in the pie chart in Fig. 1(c). The corresponding FVs of the BNN instance are plotted next to the pie chart, arranged based on their prediction: the 4 FVs in the upper green box correspond to the instances classifying the input correctly (which we refer to as $\text{Nets}_{\text{correct}}$), while the 6 FVs in the lower blue and red boxes correspond to those classifying the input wrongly (which we refer to as $\text{Nets}_{\text{wrong}}$). The networks that correspond to the FVs in the blue box wrongly predict the input as *Vegetable garden*, while the ones that correspond to the FVs in the red box wrongly predict the input as *Barn*. Comparing the FVs of $\text{Nets}_{\text{correct}}$ and $\text{Nets}_{\text{wrong}}$, we notice that most of the FVs of $\text{Nets}_{\text{wrong}}$ contain fur or farm animal-like objects such as sheep, horses and cows, while FVs of $\text{Nets}_{\text{correct}}$ do not. This implies that the 6 instances in $\text{Nets}_{\text{wrong}}$ use animals within their decision strategy to classify an image as *Farm*, and since $x^{(1)}$ does not contain any *Farm animal* concept, they can not classify it correctly. To further demonstrate that FVs can reveal the characteristics of each BNN instance, we manipulate the test sample $x^{(1)}$ by using another test sample $x^{(2)}$ which contains a very small sheep (*Farm animal* concept) and which is classify correctly by all BNN instances in $\text{Nets}_{\text{wrong}}$. From $x^{(2)}$, we cut out the the small sheep and paste it into $x^{(1)}$ manually (see $x^{(1,\text{edited})}$ in the figure). Now, all instances classify $x^{(1,\text{edited})}$ correctly as *Farm* as shown by the green pie chart. This implies that the high-level animal concepts inherent in the FVs of $\text{Nets}_{\text{wrong}}$ are indeed the concepts that the networks is searching for in the input image in order to classify an input as *Farm*. Two other examples are given in Appendix A. With this experiment we demonstrated, that the diverse decision-making strategies of different BNN model instances can indeed be explained by global XAI methods, providing evidence for our question 1) from the introduction.

4.2 Dependence on hyperparameters and initialization

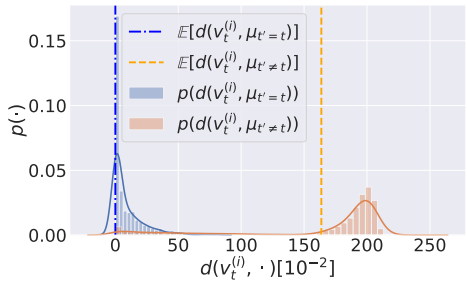

Figure 3: Distribution of distances between FVs and their corresponding instance centers (blue) and distribution of the distances between different instance centers (orange). The distances within the instances are much smaller than between different instances, and both distributions are clearly separated. This implies that the impact of parameter initialization for the AM optimization is ignorable.

The AM optimization equation 6 is highly non-convex, and therefore the obtained FVs can depend on the hyperparameter setting and parameter initialization. Hence, we would need to appropriately choose the setting such that the FVs properly extracts the concepts that the networks is using for the decision-making process. Accordingly, we investigate the dependence of FVs on the hyperparameters, e.g., the number of epochs for SGD and the step size α, and the initialization — we start from two random initial points, $v_0^{(1)}$ and $v_0^{(2)}$ to solve the optimization problem of equation 6. From the results, shown in Fig. 2, we can observe, that the AM optimization for $\alpha = 0.005$ does not converge either for 128 or 512 epochs. Futhermore, we can observe that $\alpha = 0.5$ results in over-contrasted FVs, and that different initializations can change the location and shape of the concept objects slightly. However, the content of the represented concepts are unchanged for different settings and initializations. The result implies that our approach can be used for analyzing the decision-making process without carefully tuning the parameters. Note that the location shift of concept objects by initializations might strongly affect the quantitative analysis of the diversity of BNN instances if we would adopt a naive distance measure, e.g. measuring the distance in pixel space. We will make sure in the next experiment that this is not the case when we use the distance measure introduced in Section 3.5.

4.3 Quantitative diversity of FVs

Here, we validate our quantitative distance measure in the FV space by showing that it suffices two requirements: 1) the diversity caused by parameter initializations for the AM optimization is ignorable compared to the diversity of BNN instances, and 2) the measured diversity is highly correlated to the uncertainty of the prediction. In order to evaluate 1), we first generate 5 FVs for each of 100 BNN instances and compute the average *latent concept vector* for each of the instances. We will refer to these 100 mean vectors as instance centers. In Fig. 3 we plot the histogram of the euclidean distance from each FV to its corresponding instance center (blue), as well as to another instance center (orange). We can observe a significant separation between the two histograms, implying that the FV diversity caused by initialization is indeed ignorable.

Next, we investigate the correlation between the diversity of FVs and predictive entropy. For uncertainty estimation, we use the predictive entropy:

$$H(x^*) := -\sum_{c=1}^{C} P(y^* = c|x^*, \mathcal{D}) \log P(y^* = c|x^*, \mathcal{D}).$$

We prepare 100 sets, each comprised of 100 model instances with different FVVar (see Appendix B for how to generate those sets), and plot the FV variance

$$\text{FVVar} := \frac{1}{T}\sum_{t=1}^{T} \left\| g_\phi(v_t) - \frac{1}{T}\sum_{t'=1}^{T} g_\phi(v_{t'}) \right\|_2^2 \tag{9}$$

in horizontal axis and the empirical mean predictive entropy over the whole data set $\mathcal{D}$

$$\mathbb{E}_{p(x)}[H(x)] := \frac{1}{N}\sum_{n=1}^{N} H(x^{(n)})$$

in the vertical axis in Fig. 4. Here, T is the number of BNN instances in a set, $\{v_t\}_{t=1}^T$ are the FVs of them, and the predictions (for computing the entropy) is made by those T instances. We can observe high correlation (0.83) between the FVs diversity and the uncertainty estimates, showing that our distance measure in the FV space properly reflects the distance between BNN instances. Overall, we can conclude that our distance measure suffices the two requirements above, and we now apply our tools for analyzing BNN instances.

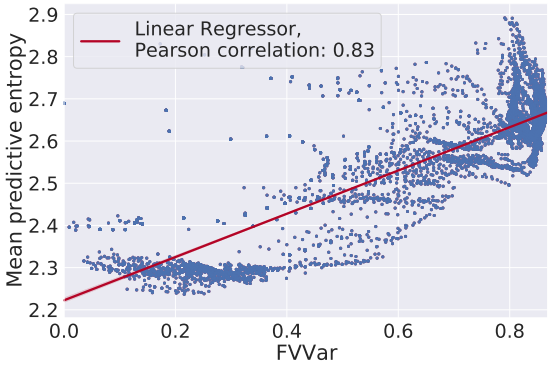

Figure 4: Linear regressor and pearson correlation between feature visualization diversity (FVVar) and mean predictive entropy. High correlation between FVVar and the mean predictive entropy is observed, as is also denoted by the positive slope of the Linear Regressor.

4.4 Comparing representations of different BNN inference methods

Here, we will visually and quantitatively compare the learned representations of models that were trained using different *Bayesian* inference methods. We train *ResNet50* on Place365 with the *Bayesian* approximation methods listed in Table 3. First, we find the cluster structure of BNN instances of each inference method, and compare their learned concepts. To this end, we compute the FV for the class *Farm* of each of the 100 BNN instances, individually. Fig. 5 shows t-SNE plots of the BNN instances in the FV space with typical FV images from each cluster for KFAC, MultiSWAG, MCDO-5% and MCDO-25%. Note that t-SNE is applied in the latent concept space, i.e., to the vectors $\{g_\phi(v_t)\}$, and therefore reflect our quantitative distance measure. Clustering is performed by applying KMeans (Lloyd, 1982) (again to the latent concept vectors $\{g_\phi(v_t)\}$), and the instances that

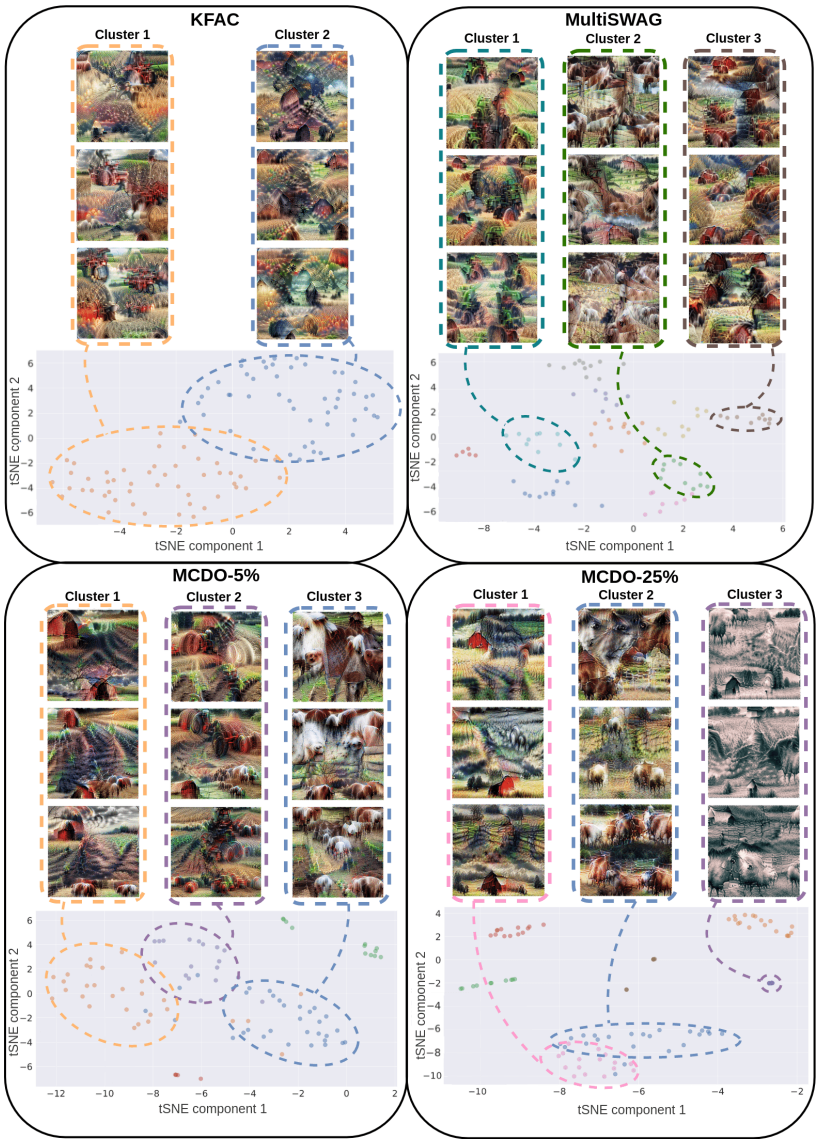

Figure 5: FVs and cluster structure of the learned concepts for class logit *Farm*. Four black box represent KFAC, MultiSWAG, MCDO-5%, and MCDO-25%, respectively. The FVs are clustered using KMeans (the number of clusters is manually chosen) and plotted in two-dimensional t-SNE space in different colors. We choose certain clusters and plot 3 example FVs of each cluster. The shown FV of a specific cluster are marked by rectangles and same-colored ellipses in the t-SNE plots. For each *Bayesian* inference method, we mostly found the following concepts in the displayed clusters. We choose certain clusters and plot 3 example FVs of each cluster. The FVs in a colored rectangle are from the cluster depicted as an ellipse in the same color in the t-SNE plot. For each *Bayesian* inference method, we mostly found the following concepts in the displayed clusters. **KFAC** cluster 1: *Tractor*, *Crop field*, and little details of animals, e.g. *Eyes*. KFAC cluster 2: *Red barn*, *Crop field*, *Pasture fence*, and little details of animals, e.g. *Eyes*. **MultiSWAG** Cluster 1: *Tractor*, *Crop field*. MultiSWAG cluster 2: *Farm animal*, *Crop field*, and *Pasture fence*. MultiSWAG cluster 3: *Red barn* and *Crop field*. **MCDO-5%** cluster 1: *Red barn*, *Crop field*. MCDO-5% cluster 2: *Tractor* and *Crop field*. MCDO-5% cluster 3: *Farm animal*, *Pasture fence*. **MCDO-25%** cluster 1: *Red barn*, *Crop field*, *Pasture fence*. MCDO-25% cluster 2: *Farm animal*, *Pasture fence*, and *Crop field*. MCDO-25% cluster 3 mostly contains a mixture of all found *Farm* concepts in a specific grayscale.

belong to different clusters are depicted in different colors. We can observe that the concepts of the class *Farm*, which are visually perceptible, generally consist of *Red barn*, *Tractor*, *Farm animal*, *Crop field*, and

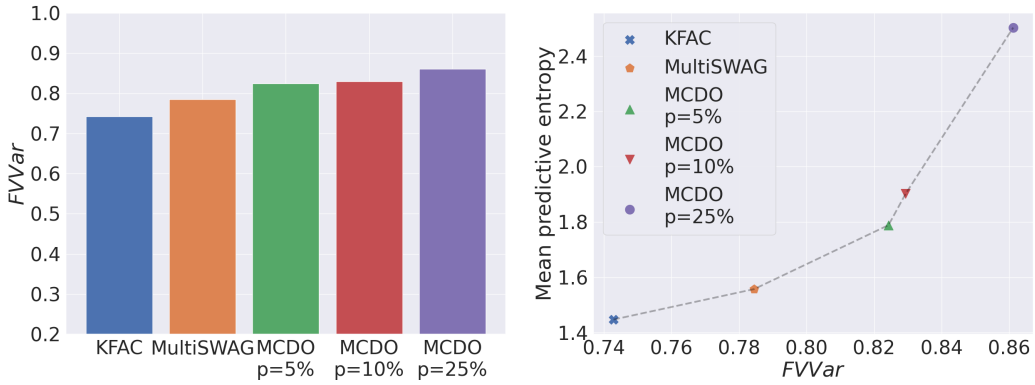

Figure 6: Representation diversity of *Bayesian* inference methods. The left subplot displays the FVVar of BNN instances of each inference method. The diversity of KFAC, MultiSWAG, MCDO 5%, 10%, and 25% is increasing from left to right. The right subplot displays the correlation between FVVar and the mean predictive entropy. They highly correlate with each other, as expected.

Pasture fence. However, different inference methods yield different cluster structures: KFAC yields 2 clusters and MultiSWAG yields ~ 10 clusters indicated by the different colors in Fig. 5 respectively. Furthermore, we can observe that MCDO yields $5 \sim 7$ clusters, while the distribution looks highly dependent on the dropout rate. KFAC yields the least diverse FVs, in terms of visual comparison, with 2 clusters, and all instances tend to include almost all of the *Farm* concepts. Nevertheless, we observe a difference between the 2 equally sized clusters which relates to the *Tractor* concept being more present in cluster 1 and the *Red barn* concept being more present in cluster 2.

The MultiSWAG instances also include different *Farm* concepts in each of the instances, however visualizing their clusters individually, we can observe that some clusters include certain concepts more frequently than the others. In particular, cluster 1 includes the *Tractor* and *Crop field*, cluster 2 the *Farm animal* and *Pasture fence*, and cluster 3 the *Red barn*, *Crop field* and *Pasture fence* concepts more frequently than the other clusters. The other 7 clusters contain all *Farm* concepts and are similar in terms of the content of concepts (see Appendix C). For MultiSWAG, the clusters found by KMeans match the MoG structure, i.e., most of the BNN instances generated from the same posterior Gaussian component are clustered together. This connects to the fact that each SWAG ensemble member converges to a different local minimum (Wilson & Izmailov, 2020), or *posterior* mode. MCDO-γ shows the most diverse FVs. We observe in Fig.5 that the BNN instances of each cluster seem to specialize with respect to certain *Farm* concepts and can be thus separated very well by these concepts. For MCDO-5%, cluster 1 primarily includes the *Red barn* and *Crop field*, cluster 2 the *Tractor* and *Crop field*, and cluster 3 the *Farm animal* and *Pasture fence* concepts. Naturally, the diversity of MCDO-γ instances increases with increasing Dropout rate, and thus MCDO-25% results in an increased number of clusters. Also, we observe that the quality of FVs decreases with increasing Dropout rate and that more diverse color schemes appear, e.g. two yellow scales, two gray scales, and one blue scale for MCDO-25%. In Appendix C, we additionally show the results for MCDO-10% and include examples of the remaining clusters of the MultiSWAG model instances. Fig. 6 shows the quantitative diversity of FVs and uncertainty of predictions, i.e., FVVar defined in Eq. equation 9. We can see in the left subplot, that the FVVar follows our qualitative observations: KFAC yields the lowest variability, followed by MultiSWAG and the MCDO 5%, 10%, 25% yields the largest diversity in this order. Hence, we can answer question 2) from the introduction "*Does the choice of the Bayesian inference method affects the diversity of their feature visualization?*" with yes.

The right subplot in Fig. 6 compares the FV diversity and the entropy. We observe, for the first time, that the FV diversity correlates with the produced uncertainty estimates of the samples. This answers question 3) from the introduction "*Can the uncertainty estimates provided by a BNN be explained by the diversity of their feature visualizations?*".

4.5 Visualizing the multimodal structure of the *posterior* distribution of BNNs.

Here we explain the multimodal structure of the BNN posterior distribution. Specifically, we use BNN instances drawn from the MoG posterior equation 5 obtained by MultiSWAG, and qualitatively (visually) and quantitatively analyze their behaviors. Furthermore, we investigate the dependence between the multimodality and the network width in terms of humanly understandable concepts using FV. To this end, we train a *WideResNet28* and its modified versions listed in Tab. 2, where *WRes*β refers to a *WRes* network, where the width is scaled by β. The models are trained on CIFAR-100 by MultiSWAG with a mixture of $K = 10$ Gaussians posteriors. After training, we draw 100 BNN instances from each Gaussian posterior, resulting in 1000 BNN instances in total, and compute their individual FVs for the class *Castle*. We plot the FV for the networks with different width in a t-SNE plot, shown in Fig. 7 at the bottom. Above, for each network, three FV from three hand-picked Gaussian distributions are shown. The black boxes indicates the different networks, i.e., *WRes*0.2, *WRes*1, and *WRes*10, respectively (Results with other networks are shown in Appendix C.1). Figure 7 shows distributions of the 1000 BNN instanecs in the FV space, where the black boxes correspond to the different networks with different widths, i.e., *WRes*0.2, *WRes*1, and *WRes*10, respectively (Results with other networks are shown in Appendix C.1). For each network, a t-SNE plot of FVs are shown in the bottom row, and FVs of three BNNs from three hand-picked modes are visualized. Note that the color in the t-SNE plot indicates the Gaussian component of MultiSWAG (KMeans is not applied here). From the t-SNE plots, we observe that the network width strongly affects the multimodal

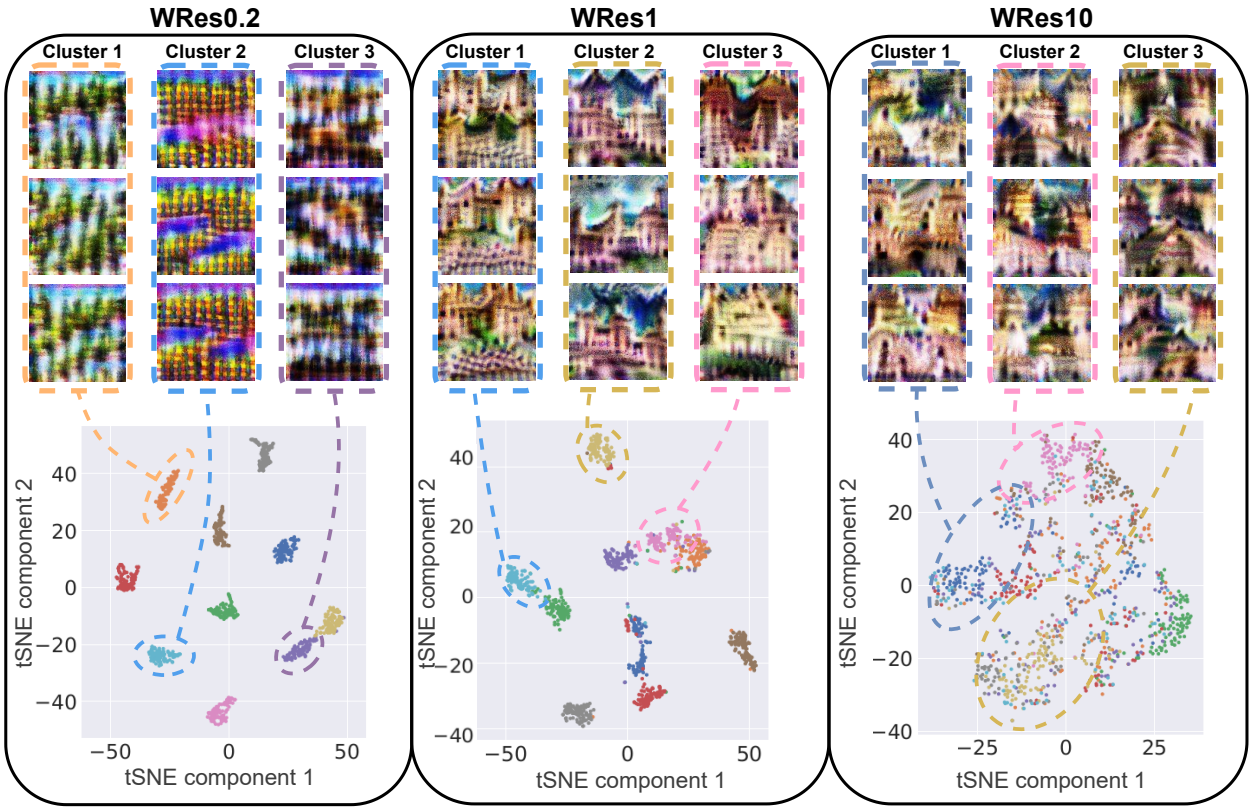

Figure 7: Multimodal sutructure of BNNs trained by MultiSWAG in the FV space. The three black bounding boxes correspond to the networks with different widths, i.e., WRes-0.2, WRes-1, and WRes-10, respectively. For each network, a t-SNE plot of 1000 BNN instances are shown in the bottom row, and FVs of three BNNs from three hand-picked SWAG modes are visualized in the top row. We observe that the modes tend to overlap as the network width increases. Moreover, the quality of FVs drastically improves from WRes0.2 to WRes1, and WRes10 successfully abstracts the castle class by replacing discrete shape information (small discrete shapes, e.g., in the bottom of WRes1 Cluster 1) by smoother ones in each mode (compare bottom of WRes10 Cluster 2).

structure: For small network width (*WRes*0.2), instances from different modes are separable, while, for wide network (*WRes*10), the instances are overlapped.

For quantifying this observation, we compute the inter-mode variance

$$\text{InterModeVar} := \frac{1}{K}\sum_{k=1}^{K}\left\|\mu_k - \frac{1}{K}\sum_{k'=1}^{K}\mu_{k'}\right\|_2^2 \tag{10}$$

and the intra-mode variance

$$\text{IntraModeVar} := \frac{1}{K}\sum_{k=1}^{K}\frac{1}{100}\sum_{t=1}^{100}\|z_{k,t} - \mu_k\|_2^2\,, \tag{11}$$

and plot them in the left panel of Fig. 8. Here, $z_{k,t}$ is the latent concept vector of the FV of the t-th instance from the k-th mode (k-th Gaussian component), and μ_k is the latent concept vector of the FV of the k-th Gaussian center. We can observe that, with a growing network width, the inter-mode variability decreases, while the intra-mode variability increases. The former (descreasing variability) aligns with the implications of recent theory on Neural Tangent Kernels (NTK) (Jacot et al., 2018; Arora et al., 2019): infinitely wide networks have a global solution close to any initial point in the parameter space, and all those global solutions behave/perform similarly—the modes that behave similarly should have similar FVs. On the other hand, to the best of our knowledge, the latter (increasing intra-mode variability with growing β) is not explained by theory so far.

In the following, we will answer question 4) from the introduction regarding the impact of the network width on the diversity of FV of samples from a multimodal posterior distribution. To this end, we first qualitatively investigate the FVs given in Fig. 7. We can observe that a too narrow network (*WRes*0.2) gives notably low quality FVs, which implies that the network does not have sufficient capacity to learn good feature representations. As a result, the network only learns simple concepts, i.e., patterns like stripes and grids, instead of the high-level *Castle* concepts, e.g. *castle tower*. The large inter-mode variability reflects the fact that each mode learns different color schemes and different patterns, while the small intra-mode variability results in identical concepts within each mode. For larger network widths, we observe a clear difference in their FVs. Modes of WRes1 still learn different color schemes, and at the same time also learn high-level *Castle* concepts, e.g. *castle towers* with different colors. In each mode, we can observe intra-mode variability as the difference in the *shape* of the castle towers. Modes of WRes10 leans very similar features of more abstract castle concepts, i.e., the shape information is reduced, and it is harder to distinguish the FV of the different modes.

The difference between WRes1 and WRes10 implies that, for a moderate network width, each mode plays different roles and searches for different shapes of the class objects, while, for a large network width, modes get mixed and each mode abstracts the concepts well, such that a single model alone can perform well in terms of test accuracy and test calibration, e.g. ECE. We test this implication by checking how strongly the application of ensembling impacts the performance of the average SWAG models, compared to the performance of their ensemble, e.g. MultiSWAG. In the right panel of Fig. 8 we plot the MultiSWAG test accuracy, subtracted by the average SWAG model accuracy, and the MultiSWAG test ECE, subtracted by the average SWAG model test ECE, for each of the WRes models, respectively. We observe an improvement of test accuracy for growing width models, e.g. WRes0.2 to WRes1, by applying ensembling. Increasing the model widths further, i.e. WRes1 to WRes10, however, results in decreasing test accuracy improvements and thus a lower impact of applying ensembling. For test ECE we can see that ensembling yields a larger benefit, in terms of test ECE, for larger width models. Our observations suggests that for a reasonable network width, e.g. WRes1, each ensemble member learns different specialized concepts that are used for prediction and thus the test accuracy and test ECE improve more when ensembling, than for WRes10, where the modes overlap, and each mode learns a variety of reasonable concepts that are important for prediction, instead of specializing in just some. The fact that ensembling yields a lower test accuracy improvement for the WRes0.2 model than for the WRes1 based mode puts forward that an overspecialization of modes (WRes0.2), e.g. each instance within a mode looks exactly the same while instances from different modes look completely different, results in a worse consensus and thus lower performance improvement when ensembling is applied, compared to modes that contain more variability between their instances, while still being diverse between modes (WRes1). Overall, we extensively showed how the width of the underlying network architecture affects

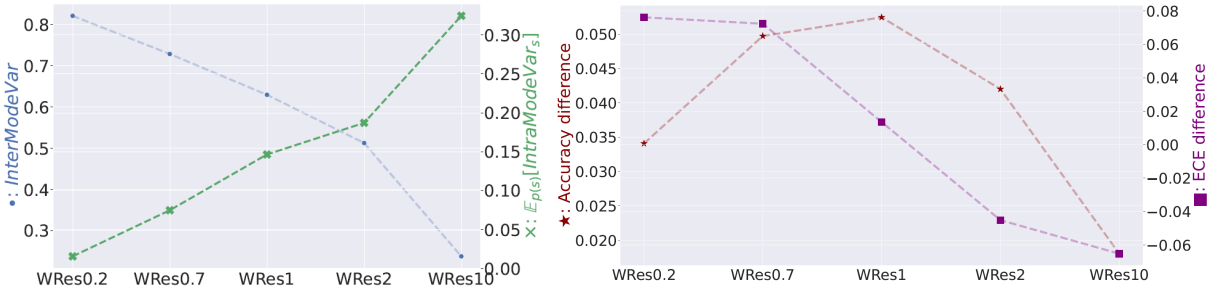

Figure 8: The left subplot shows how the inter- and intra-mode variabilities change with increasing network width. As the network width increases (from left to right), the inter-mode variability decreases, while the intra-mode variability increases. The right subplot shows the differences between the test accuracies of the ensemble of SWAG models, i.e. MultiSWAG, and the average SWAG model, as well as the differences between the ECEs of MultiSWAG and the average SWAG model. The application of ensembling yields lower test accuracy improvements for narrower models up from WRes10 to WRes1. For the WRes0.2 to WRes1 based models the test accuracy improvement increases with growing width. On the other hand, the application of ensembling yields higher test ECE improvements for growing width models from WRes1 to WRes10.

the produced FVs, answering question 4) in the introduction "*How does the network width affects the diversity of explanations of samples from a multimodal posterior distribution?*".

5 Conclusion

Since BNNs provide additional information about the uncertainty of a prediction, they are of enormous value, especially in safety-critical applications. Their ability to estimate uncertainties of a prediction is inherent in the learned multimodal *posterior* distribution. Sampling from this *posterior* distribution results in BNN instances, exhibitting diverse representations, which in turn lead to different prediction strategies. It has been shown in a large number of works that the diversity of these strategies depends on various factors, such as the choice of the Bayesian approximation method, the parameter initialization, or the model size. However, so far, this diversity has been analyzed either in the output, or parameter space of the BNN instances, which unfortunately still lacks human understandable intuition. With this work, we now deliver this missing but important building block to support human understanding by making the learned strategies visually accessible. To this end, we use feature visualizations as a global explanation method to explain — in a human-understandable way — the different representations and prediction strategies learned by BNN instances. Furthermore, this enables us to examine the diversity of the BNN instances on the feature visualizations both qualitatively and quantitatively, thus adding the visual component to the previous analysis.

In order to quantitatively analyze the FVs with their pronounced heterogeneity, we first learn a suitable representation of the FV with the help of contrastive learning, which we can then use to measure the distance. The ability to measure the distances between FVs allows us to investigate and at the same time to visually understand how the use of different *Bayesian* inference methods affects the diversity of BNN instances. Indeed, we could demonstrate, that the learned representations vary stronger for multimodal *Bayesian* inference methods, such as MultiSWAG than for unimodal ones, such as KFAC. The greatest variety of learned representations is achieved by Dropout-based models. Here the dropout rate correlated positively with the variety of representations, i.e. the higher the dropout rate, the more different the representations visible through their FVs. Furthermore, we showed that the diversity of FVs of BNN samples is positively correlated with the uncertainty estimates that we obtain from this BNN.

Moreover, we were able to measure — and visually demonstrate — the dependence of the multimodal structure of the *posterior* distribution on the width of the underlying network. Specifically, we have shown that the modes in a multimodal *posterior* distribution of MultiSWAG become more similar with increasing

width of the underlying network. This result is consistent with recent theoretical insights into Neural Tangent Kernels, where it was shown that the local solutions of infinitely wide networks behave similarly despite different initial parametrization. However, by adding the additional visual component - through the lens of *global* explanations - we can easily understand the similar behavior of the modes given their similar FVs. In future work, we will investigate how the observed behavior of *posterior* modes can help to improve model performance in detecting OOD samples.

References

Sanjeev Arora, Simon Du, Wei Hu, Zhiyuan Li, Ruslan Salakhutdinov, and Ruosong Wang. On exact computation with an infinitely wide neural net, 04 2019.

Anish Athalye, Logan Engstrom, Andrew Ilyas, and Kevin Kwok. Synthesizing robust adversarial examples. 07 2017.

David Bau, Jun-Yan Zhu, Hendrik Strobelt, Agata Lapedriza, Bolei Zhou, and Antonio Torralba. Understanding the role of individual units in a deep neural network. *Proceedings of the National Academy of Sciences*, 117:201907375, 09 2020. doi: 10.1073/pnas.1907375117.

Felix Berkenkamp, Matteo Turchetta, Angela Schoellig, and Andreas Krause. Safe model-based reinforcement learning with stability guarantees. 12 2017.

Charles Blundell, Julien Cornebise, Koray Kavukcuoglu, and Daan Wierstra. Weight uncertainty in neural networks. 05 2015.

Kirill Bykov, Anna Hedström, Shinichi Nakajima, and Marina Höhne. Noisegrad: enhancing explanations by introducing stochasticity to model weights, 06 2021a.

Kirill Bykov, Marina Höhne, Adelaida Creosteanu, Klaus-Robert Müller, Frederick Klauschen, Shinichi Nakajima, and Marius Kloft. Explaining bayesian neural networks, 08 2021b.

Ting Chen, Simon Kornblith, Mohammad Norouzi, and Geoffrey Hinton. A simple framework for contrastive learning of visual representations, 02 2020.

Yarin Gal and Zoubin Ghahramani. Dropout as a bayesian approximation: Representing model uncertainty in deep learning. *Proceedings of The 33rd International Conference on Machine Learning*, 06 2015.

Ian Goodfellow, Jonathon Shlens, and Christian Szegedy. Explaining and harnessing adversarial examples. *arXiv 1412.6572*, 12 2014.

Alex Graves. Practical variational inference for neural networks. *NIPS*, 25, 10 2021.

Kaiming He, Xiangyu Zhang, Shaoqing Ren, and Jian Sun. Deep residual learning for image recognition. 7, 12 2015.

Jacob Hilton, Nick Cammarata, Shan Carter, Gabriel Goh, and Chris Olah. Understanding rl vision. *Distill*, 2020. doi: 10.23915/distill.00029. https://distill.pub/2020/understanding-rl-vision.

Yu Huang and Yue Chen. Autonomous driving with deep learning: A survey of state-of-art technologies, 06 2020.

Pavel Izmailov, Polina Kirichenko, Nate Gruver, and Andrew Gordon Wilson. On feature learning in the presence of spurious correlations, 2022. URL `https://arxiv.org/abs/2210.11369`.

Arthur Jacot, Franck Gabriel, and Clément Hongler. Neural tangent kernel: Convergence and generalization in neural networks, 06 2018.

Been Kim, Justin Gilmer, Fernanda Viegas, Ulfar Erlingsson, and Martin Wattenberg. Tcav: Relative concept importance testing with linear concept activation vectors. 11 2017.

Pang Koh, Thao Nguyen, Yew Tang, Stephen Mussmann, Emma Pierson, Been Kim, and Percy Liang. Concept bottleneck models, 07 2020.

Balaji Lakshminarayanan, Alexander Pritzel, and Charles Blundell. Simple and scalable predictive uncertainty estimation using deep ensembles. 12 2016.

Sebastian Lapuschkin, Alexander Binder, Grégoire Montavon, Frederick Klauschen, Klaus-Robert Müller, and Wojciech Samek. On pixel-wise explanations for non-linear classifier decisions by layer-wise relevance propagation. *PLoS ONE*, 10:e0130140, 07 2015. doi: 10.1371/journal.pone.0130140.

Sebastian Lapuschkin, Stephan Wäldchen, Alexander Binder, Grégoire Montavon, Wojciech Samek, and Klaus-Robert Müller. Unmasking clever hans predictors and assessing what machines really learn. *Nature Communications*, 10, 03 2019. doi: 10.1038/s41467-019-08987-4.

An Le, Philipp Kratzer, Simon Hagenmayer, Marc Toussaint, and Jim Mainprice. Hierarchical human-motion prediction and logic-geometric programming for minimal interference human-robot tasks. pp. 7–14, 08 2021. doi: 10.1109/RO-MAN50785.2021.9515539.

Yann Lecun, Leon Bottou, Y. Bengio, and Patrick Haffner. Gradient-based learning applied to document recognition. *Proceedings of the IEEE*, 86:2278 – 2324, 12 1998. doi: 10.1109/5.726791.

Junnan Li, Pan Zhou, Caiming Xiong, Richard Socher, and Steven Hoi. Prototypical contrastive learning of unsupervised representations, 05 2020a.

Yunfan Li, Peng Hu, Zitao Liu, Dezhong Peng, Joey Zhou, and Xi Peng. Contrastive clustering, 09 2020b.

S. Lloyd. Least square quantization in pcm. *IEEE Transactions on Information Theory - TIT*, 28, 01 1982.

David Mackay, John Bridle, Peter Cheeseman, Sidney Fels, Steve Gull, Andreas Herz, John Hopfield, Doug Kerns, Allen Knutsen, David Koerner, Mike Lewicki, Tom Loredo, Steve Luttrell, Ken Rose, Sibusiso Sibisi, John Skilling, Haim Sompolinsky, and Nick Weir. Bayesian methods for adaptive models. 05 1999.

Wesley Maddox, Timur Garipov, Pavel Izmailov, Dmitry Vetrov, and Andrew Wilson. A simple baseline for bayesian uncertainty in deep learning, 02 2019.

James Martens and Roger Grosse. Optimizing neural networks with kronecker-factored approximate curvature. 03 2015.

L. Medsker and Lakhmi Jain. Recurrent neural networks: Design and applications. 01 1999.

Alexander Mordvintsev, Nicola Pezzotti, Ludwig Schubert, and Chris Olah. Differentiable image parameterizations. *Distill*, 2018. doi: 10.23915/distill.00012. https://distill.pub/2018/differentiable-parameterizations.

Radford Neal and M Neal. Bayesian learning for neural networks bayesian learning for neural networks. 10 2021.

Anh Nguyen, Alexey Dosovitskiy, Jason Yosinski, Thomas Brox, and Jeff Clune. Synthesizing the preferred inputs for neurons in neural networks via deep generator networks. 05 2016.

Chris Olah, Alexander Mordvintsev, and Ludwig Schubert. Feature visualization. *Distill*, 2017. doi: 10.23915/distill.00007. https://distill.pub/2017/feature-visualization.

Chris Olah, Arvind Satyanarayan, Ian Johnson, Shan Carter, Ludwig Schubert, Katherine Ye, and Alexander Mordvintsev. The building blocks of interpretability. *Distill*, 2018. doi: 10.23915/distill.00010. https://distill.pub/2018/building-blocks.

E. Pearson, Maurice Kendall, and Alan Stuart. The advanced theory of statistics. volume i, distribution theory. *Biometrika*, 46, 03 1959. doi: 10.2307/2333551.

Christian Reimers, Jakob Runge, and Joachim Denzler. *Determining the Relevance of Features for Deep Neural Networks*, pp. 330–346. 11 2020. ISBN 978-3-030-58573-0. doi: 10.1007/978-3-030-58574-7_20.

Marco Tulio Ribeiro, Sameer Singh, and Carlos Guestrin. "why should i trust you?" explaining the predictions of any classifier. In *Proceedings of the 22nd ACM SIGKDD international conference on knowledge discovery and data mining*, pp. 1135–1144, 2016.

Daniel A. Roberts, Sho Yaida, and Boris Hanin. The principles of deep learning theory, 2021.

Ramprasaath Rs, Michael Cogswell, Abhishek Das, Ramakrishna Vedantam, Devi Parikh, and Dhruv Batra. Grad-cam: Visual explanations from deep networks via gradient-based localization. pp. 618–626, 10 2017. doi: 10.1109/ICCV.2017.74.

Thomas Schnake, Oliver Eberle, Jonas Lederer, Shinichi Nakajima, Kristof Schütt, Klaus-Robert Mueller, and Gregoire Montavon. Higher-order explanations of graph neural networks via relevant walks. *IEEE Transactions on Pattern Analysis and Machine Intelligence*, PP:1–1, 09 2021. doi: 10.1109/TPAMI.2021.3115452.

Karen Simonyan, Andrea Vedaldi, and Andrew Zisserman. Deep inside convolutional networks: Visualising image classification models and saliency maps. *preprint*, 12 2013.

Daniel Smilkov, Nikhil Thorat, Been Kim, Fernanda Viégas, and Martin Wattenberg. Smoothgrad: removing noise by adding noise. 06 2017.

Mukund Sundararajan, Ankur Taly, and Qiqi Yan. Axiomatic attribution for deep networks. 03 2017.

Christian Szegedy, Wojciech Zaremba, Ilya Sutskever, Joan Bruna, Dumitru Erhan, Ian Goodfellow, and Rob Fergus. Intriguing properties of neural networks. 12 2013.

Tatiana Tommasi, Novi Patricia, Barbara Caputo, and Tinne Tuytelaars. *A Deeper Look at Dataset Bias*, pp. 37–55. 09 2017. ISBN 978-3-319-58346-4. doi: 10.1007/978-3-319-58347-1_2.

Nicol Turner Lee. Detecting racial bias in algorithms and machine learning. *Journal of Information, Communication and Ethics in Society*, 16, 09 2018. doi: 10.1108/JICES-06-2018-0056.

Andrew Wilson and Pavel Izmailov. Bayesian deep learning and a probabilistic perspective of generalization, 02 2020.

Sergey Zagoruyko and Nikos Komodakis. Wide residual networks. 05 2016.

Ruqi Zhang, Chunyuan Li, Jianyi Zhang, Changyou Chen, and Andrew Wilson. Cyclical stochastic gradient mcmc for bayesian deep learning, 02 2019.

A Decision-making strategy manipulation

In the introductory experiment in Section 4.1, we demonstrate that we can visualize and extract high-level information about the decision-making strategies of BNN instances from FV and, for the first time, visualize their differences. Here we show a few other examples in Fig.9.

B Constructing FV diversity sets

Here, we explain how we formed the sets of BNN instances used in sec. 4.3, where the correlation between the FV diversity, FVVar, and the mean predictive entropy is evaluated. We first prepared a pool $\Theta := \{\theta_t | t = 1, ..., T_{total}\}$ of BNN instances, by drawing samples from the posterior distribution. From Θ, we generated 100 different sets $\{S_i | i = 1, \ldots, 100\}$, each of which consists of 100 BNN instances. Each set S_i collects samples from Θ in the following way: after randomly choosing the first instance $\theta^1_{S_i} \in \Theta$, we iteratively add the nearest neighbor (in the FV metric space) of the last added instance $\theta^{t-1}_{S_i}$ for $t = 1, \ldots, 100$. Note that, every time we added an instance to a set, the corresponding instance is removed from the pool, i.e., $\Theta \leftarrow \Theta \setminus \theta^t_{S_i}$. Although we did not control the diversity of each set, the resulting sets had different diversity as shown in figure 4.

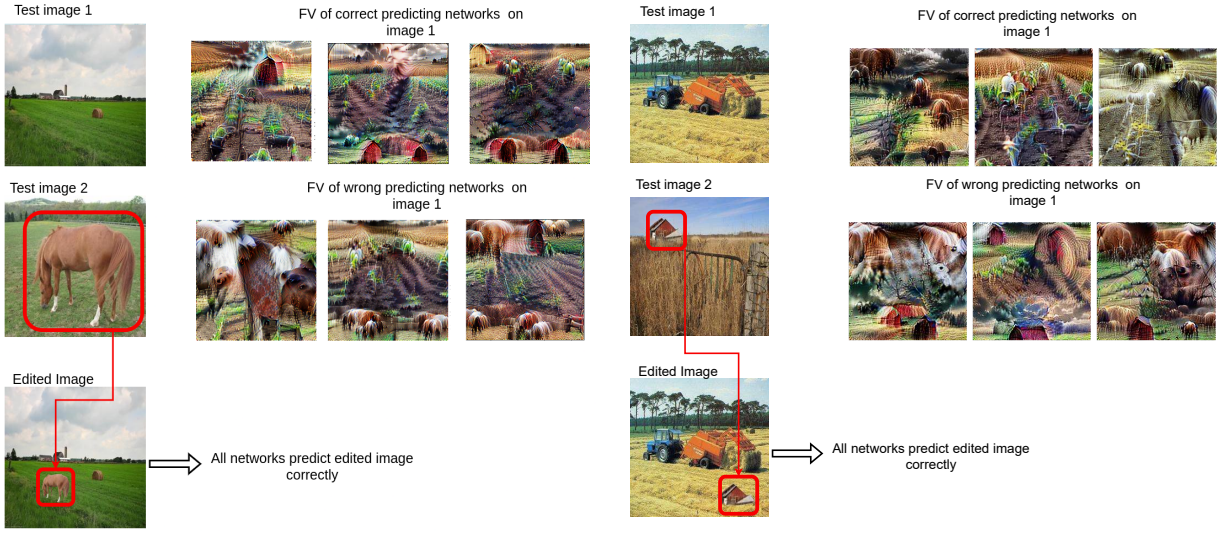

Figure 9: Two additional image manipulation examples. **Left:** In this example we can see that the selected images that predicted "Test image 1" correctly include the high-level concepts *Red barn* and *Crop fields*, which are also present in the image. On the other hand, the chosen networks that predicted the image incorrectly, include the high-level concept *Farm animal* in them. After manipulating Test image 1 by pasting a horse (*Farm animal*) from "Test image 2" of the test set, all networks do predict the "Edited image" correctly. **Right:** In this example we can see that the selected images that predicted "Test image 1" correctly include the high-level concept *Crop field*, which are also present in the image. On the other hand, the chosen networks that predicted the image incorrectly, include the high-level concept *Red barn* in them. After manipulating Test image 1 by pasting a red barn from "Test image 2" of the test set, all networks do predict the "Edited image" correctly.

C Clustering representations of different BNN inference methods

For the experiments in sec. 4.4 we cluster the FVs by applying KMeans. We choose the number of clusters by qualitatively analyzing the goodness of clusters, that is, whether the points cluster well in the t-SNE plots, and whether human-understandable concepts, e.g. *Farm animal*, are clustered together. We show the t-SNE plots for the MCDO-10% model in Fig.10, the FVs of MCDO-10% in Fig.11, and the FVs of the MultiSWAG clusters in Fig.12.

C.1 Multimodal structure of the posterior distribution of BNNs - WRes0.7 and WRes2.

In Fig. 13 we show the t-SNE plots and respective FVs of some example clusters of the WRes0.7 and WRes 2 models. As can be seen, the FVs are naturally clustered together and well separated for the narrower WRes0.7 model, and overlap more for the WRes2 model.

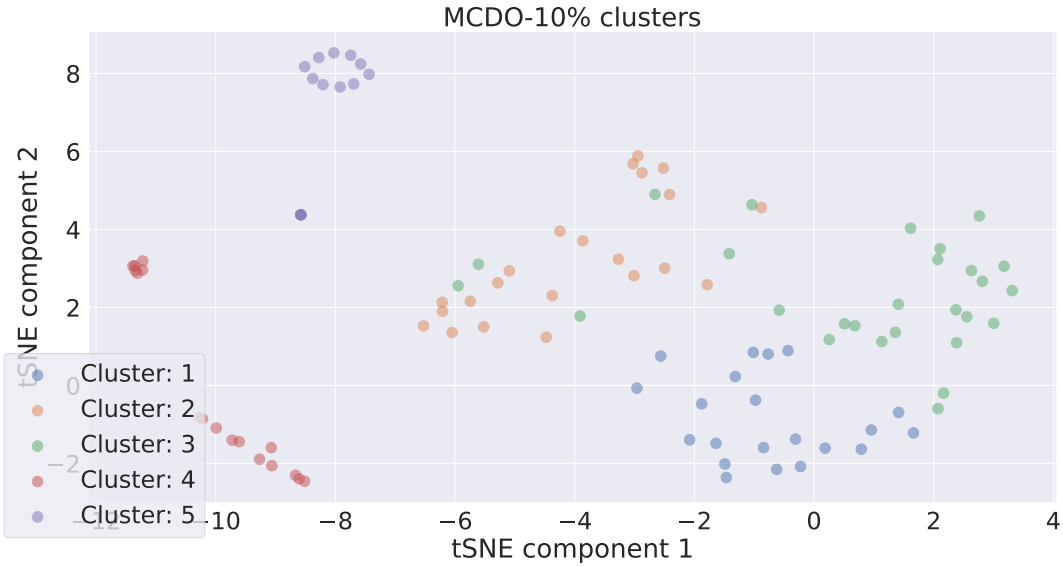

Figure 10: MCDO-10% clusters. The instances cluster into 5 clusters, of which two, Clusters 1 and 4, are well separated, while the other three, Clusters 2, 3, and 5, are connected.

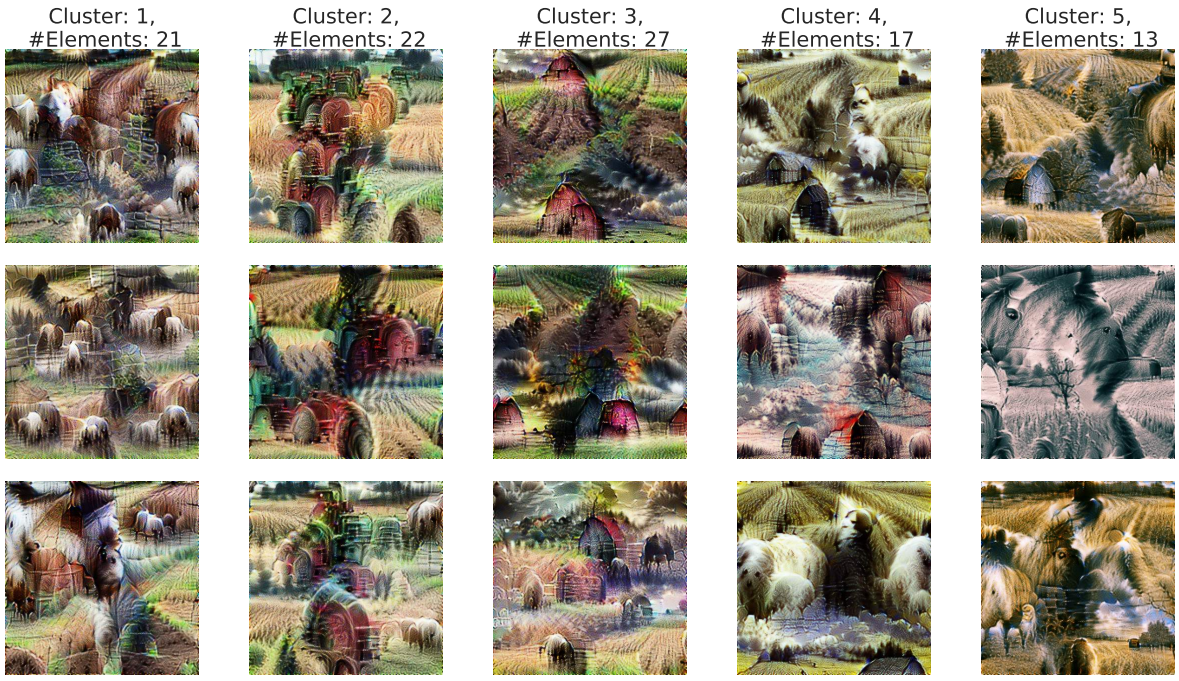

Figure 11: Five clusters formed by MCDO-10%. Clusters 1-3 are connected, and similar in terms of their color scheme. However, Cluster 1 contains the *Farm animal*, Cluster 2 the *Tractor*, and Cluster 3 the *Red barn* concepts more frequently than the others. The other two clusters, Clusters 4 and 5, contain a mix of all *Farm* concepts, however in a different color scheme.

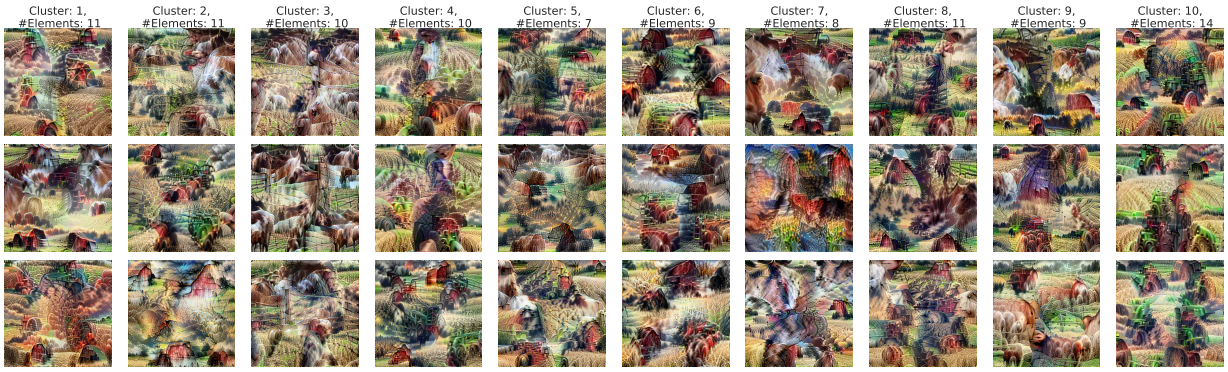

Figure 12: MultiSWAG clusters. The MultiSWAG clusters mostly cluster with regards to the underlying SWAG ensemble members. We can see, that most clusters contian a variety of *Farm* concepts in them.

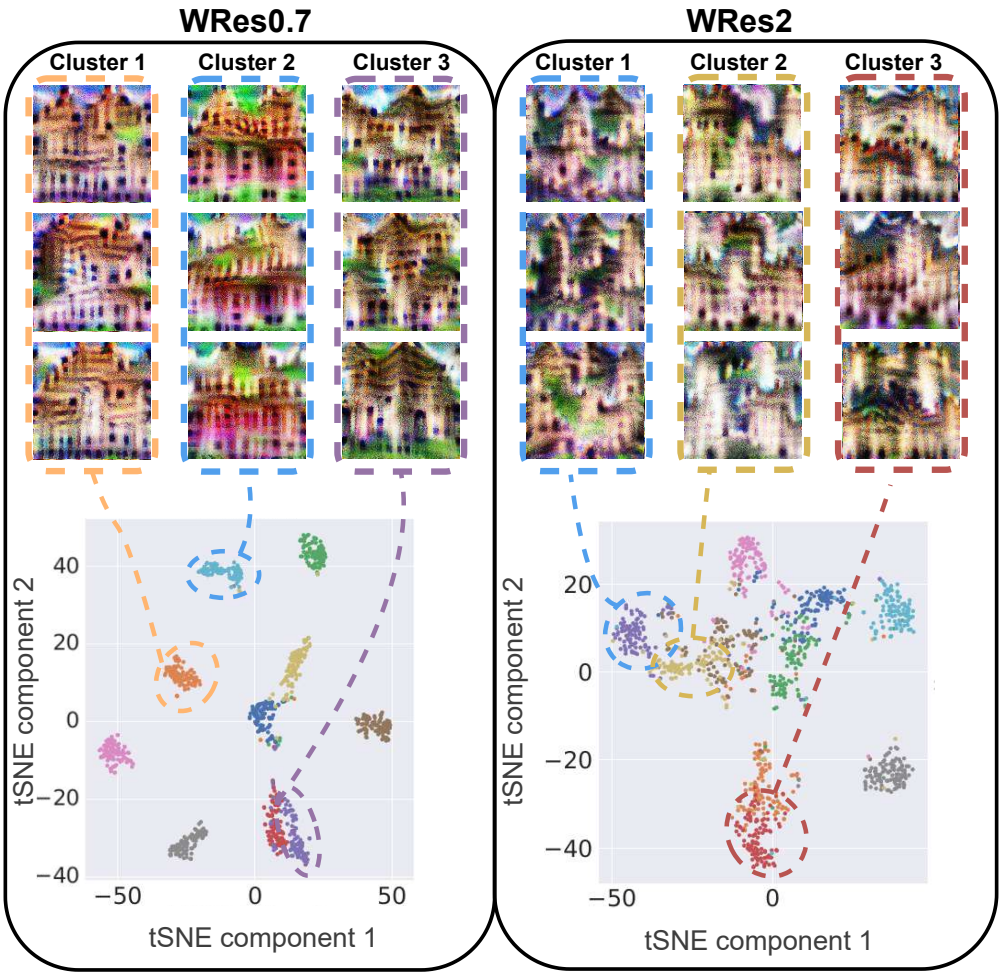

Figure 13: Multimodal structure of WReNet28 with different network width in the FV space. The black bounding box corresponds to WRes-0.7, and WRes-2. The colored dashed bounding boxes mark FVs of 3 BNN instances from 3 modes. As the network width increases, the modes overlap more.